D-orbital electronic configuration-dependent photocatalytic CO_2 reduction activity of noble metal-free terpyridine-based supramolecular assemblies

Jia Song [a], Shanchao Wang [a], Lin Wang [a,*], Qingzhi Luo [a], Jing An [a], Yandong Duan [a], Desong Wang [a,b,**]

[a] Hebei Key Lab of Photoelectric Control on Surface and Interface, College of Sciences, Hebei University of Science and Technology, Shijiazhuang 050018, People's Republic of China
[b] State Key Lab of Metastable Materials Science and Technology, Hebei Key Lab of Applied Chemistry, Yanshan University, Qinhuangdao 066004, People's Republic of China

ARTICLE INFO

ABSTRACT

Coordination non-noble metal ions in terpyridine-based supramolecular photocatalysts can promote the charge directional transfer towards metals and reduce the enriched CO_2. Whether all non-noble metal can play this role and how the electronic structure of metal regulates the activity? Here, a series of photocatalysts were constructed by self-assembly of terpyridine-based molecules and non-noble metals (Zn^{2+}, Co^{2+}, Ni^{2+} and Cd^{2+}) through coordination interactions and π-π stacking interactions. Study results showed that unpaired d electrons in Co^{2+} and Ni^{2+} induce photogenerated electrons deactivation which cannot be used for CO_2 reduction through ligand to metal charge transfer (LMCT) process, reflected in low CO evolution rates of 4.07 and 4.30 μmol g^{-1} h^{-1}. However, Zn^{2+} and Cd^{2+} with filled d^{10} configurations do not participate in LMCT and activities improve to 46.54 and 38.51 μmol g^{-1} h^{-1}. This work offers guidance for designing an efficient photocatalyst by tuning the central metals.

1. Introduction

With the consumption of fossil fuels, the emission of CO_2 has severely increased, leading to urgent energy shortages and environmental issues [1]. Photocatalytic CO_2 reduction is one of the most promising strategies to relieve energy and environmental crisis in the way of capturing and converting CO_2 into value-added chemicals and fuels, such as CO, CH_4, CH_3OH, etc [2]. The key part of this strategy is to develop sufficiently efficient and low-cost photocatalysts. Supramolecular organic photocatalyst was deemed as a prospective photocatalyst owing to the advantages of abundant element resource, structure versatility and band gap tunability etc [3]. They can be easily constructed by self-assembly of π-conjugated molecules, including perylene diimide [4], porphyrin [5], phthalocyanine [6], fullerene [7], pyridine [8], and their derivatives through noncovalent bond interactions, *e.g.* π-π interactions, hydrogen bonds, hydrophobic interactions, electrostatic interactions, avoiding the fussy synthesis procedures and rigorous reaction conditions [9]. The delocalized π electrons flow along the π-π stacking direction, endowing

the assemblies with semiconductor property. Whereas, common π-conjugated porphyrin and perylene diimide assemblies usually have narrow band gaps and positive conduction band (CB) potentials, which adverse to the electron and holes separation, and do not possess enough negative reduction potential to reduce CO_2 [10–12]. An example of that perylene diimide (PDI) assembled photocatalyst has no ability to reduce CO_2 because of its CB potential near zero [13].

2, 2′:6′,2″-terpyridine (tpy) has attracted great attention by virtue of the synthetic accessibility and strong electron affinity arising from its electron-deficient property. Taking advantage of the electron-deficient characteristic, terpyridine can be utilized as "acceptor" to construct donor-acceptor photocatalysts, and electrons migrate toward the "acceptor" directly, thus more electrons can be separated and generated during the CO_2 reduction [14,15]. Meanwhile, based on our previous work, we found the terpyridine-based assemblies possess the depth negative CB potential and have better CO_2 reduction potential [16]. Furthermore, terpyridine rings have excellent coordination ability with transition metals owing to the suitably arranged nitrogens in three

---

pyridine rings, so terpyridines are powerful building block in constructing metallo-supramolecular assemblies. Coordinated transition metals were believed to functionalized sites for absorbing and activating more CO_2 molecules [17], and they can further reinforce electron-deficient property of the terpyridine rings, boosting more charge directional transfer toward the metal ions and exact reduction of the enriched CO_2 in here [18,19]. Thus, the central metal of terpyridine not only is absorption site but also is the catalytic site, which can achieve the "One stone and Two birds" effect and thus enhance the reduction activity. Noble transition metals, such as Ru, Re and Ir are high cost and low abundance [20,21], thus, from the point of view of sustainable development, photocatalysts based on earth-abundant metals are more appealing. For example, Maji synthesized a coordinated polymer (TPA-Zn) by Zn(II)-assisted self-assembly of triphenylamine (TPA) cored tristerpyridine ligand [22]. The Zn(II) metal nodes provide a suitable amount of exciton separation and charge carrier mobility, facilitating the improvement of photocatalytic activity. Subsequently, this group continued to prepare coordination polymer gels by the self-assembly of Zn(II) with one linker of tetrathiafulvalene and terpyridine derivative (TPY-TTF) [23], and one linker of anthracene-terpyridine based molecules (TPY-ANT) [14], respectively, both of which exhibit high photocatalytic activities toward H_2 production and CO_2 reduction. The above examples mainly concentrated on preparing and studying zinc coordinated photocatalysts. Whether all non-noble transition metals can play this role like Zn(II) has no study, systematic comparison of photocatalytic activities of terpyridine-based assemblies coordinated with different metals has not been done and how the electronic structure of metal regulates the photocatalytic activity remains unclear. Thus, an in-depth fundamental understanding of central metal and photocatalytic activity relationships is indispensable to rationally design supramolecular photocatalysts and tune their structure for an intended application.

Based on the above consideration, a series of metallo-supramolecular photocatalysts were constructed *via* coordination-driven self-assembly of earth-abundant metal (Zn^{2+}, Co^{2+}, Ni^{2+} and Cd^{2+}) and 4′-(4-Bromophenyl)− 2,2′:6′,2''-terpyridine (Brphtpy) based on coordination interactions and π-π stacking interactions. Brphtpy molecules were chosen as ligands because they were facilely synthesized and possess conjugated rigid structure which easily self-aggregates to organic semiconductor through intermolecular π-π interactions. The structure diversity of metal offers an opportunity to investigate the effect of electronic configurations on photocatalytic CO_2 reduction. Electron paramagnetic resonance (EPR) spectroscopy, high-resolution electrospray ionization mass spectroscopy (HR-ESI-MS), and crystal-field theory revealed the electronic configurations of central metals. Photoelectric characterizations together with DFT calculations systematically showed how the electronic configuration of central metals regulates the light absorption, energy structure, charge separation, and further influence the photocatalytic CO_2 reduction activity. Overall, knowing more about the structure-property relationship of central metal and photocatalytic CO_2 reduction is beneficial to designing and developing metallo-supramolecular photocatalysts with superior photocatalytic activity.

2. Experimental section

2.1. Materials

2-Acetylpyridine ($C_5H_4NCOCH_3$, 98%) was purchased from Shanghai Sun Chemical Technology Co. Ltd. 4-Bromobenzaldehyde (BrC_6H_4CHO, 99%) was obtained from Shanghai Aladdin Technology Co. Ltd. Ammonia solution ($NH_3 \cdot H_2O$, 28.0%) and absolute ethanol (CH_3CH_2OH, 98%) were both bought from Damao Chemical Reagent Factory. $Zn(NO_3)_2 \cdot 6 H_2O$, $Co(NO_3)_2 \cdot 6 H_2O$, and $Ni(NO_3)_2 \cdot 6 H_2O$ were purchased from Liaoning Cook Biotechnology Co. Ltd. All chemicals and solvents are analytical grade and used without any further purification.

2.2. The preparation of Brphtpy

The 4′-(4-Bromophenyl)− 2,2′:6′,2''-terpyridine (Brphtpy) was successfully synthesized by following procedures (Fig. S1). 2-acetylpyridine (4.86 mL, 44.0 mmol), KOH (3.40 g, 60.6 mmol), and concentrated NH_4OH (80 mL, 28.0%) were continuously added to the stirring solution of 4-bromobenzaldehyde (4.00 g, 22.0 mmol) in 50 mL of ethanol. After refluxing for 24 h, the formed precipitate was filtered, washed with ethanol three times, and collected after drying at 60 °C for 6 h. The structure of Brphtpy was confirmed by ^{1}HNMR (Fig. S2). ^{1}H-NMR (500 MHz, CDCl$_3$) : δ = 8.73 (d, 2 H, terpyridine g, n-H), 8.70 (s, 2 H, terpyridine c, j-H), 8.67 (d, 2 H, terpyridine d, k-H), 7.88 (t, 2 H, terpyridine e, l-H), 7.78 (d, J=7.7 Hz, 2 H, bromophenyl a, h-H), 7.64 (d, 2 H, bromophenyl b, i-H), 7.36 (m, 2 H, terpyridine f, m-2 H).

2.3. The preparation of [M(Brphtpy)₂] (NO₃)₂ photocatalysts

[Zn(Brphtpy)$_2$](NO$_3$)$_2$ photocatalyst was prepared according to Fig. S3. Brphtpy (200 mg, 0.515 mmol) was dissolved in 6.67 mL of CH_2Cl_2. Then, $Zn(NO_3)_2 \cdot 6 H_2O$ (153 mg, 0.515 mmol) in 4.66 mL of methanol was added to the above solution under stirring. The mixture was reacted at room temperature for 24 h, and the white solid precipitate was obtained after filtration. After the white precipitate was washed with ethanol and CH_2Cl_2 for two times, respectively, then dried at 60 °C for 6 h, the goal product was successfully synthesized. Other metallo-supramolecular photocatalysts were prepared according to the same procedures. Proper single crystal of [Zn(Brphtpy)$_2$](NO$_3$)$_2$ was chosen to study its structure by the single-crystal X-ray diffraction. The ICP-OES results reveal that the actual amounts of Zn, Co, Ni and Cd are 6.6, 6.0, 6.0,10.9 *wt*.%, which are near to the theoretical amounts of 6.7, 6.2, 6.2 and 11.0 *wt*.%, respectively.
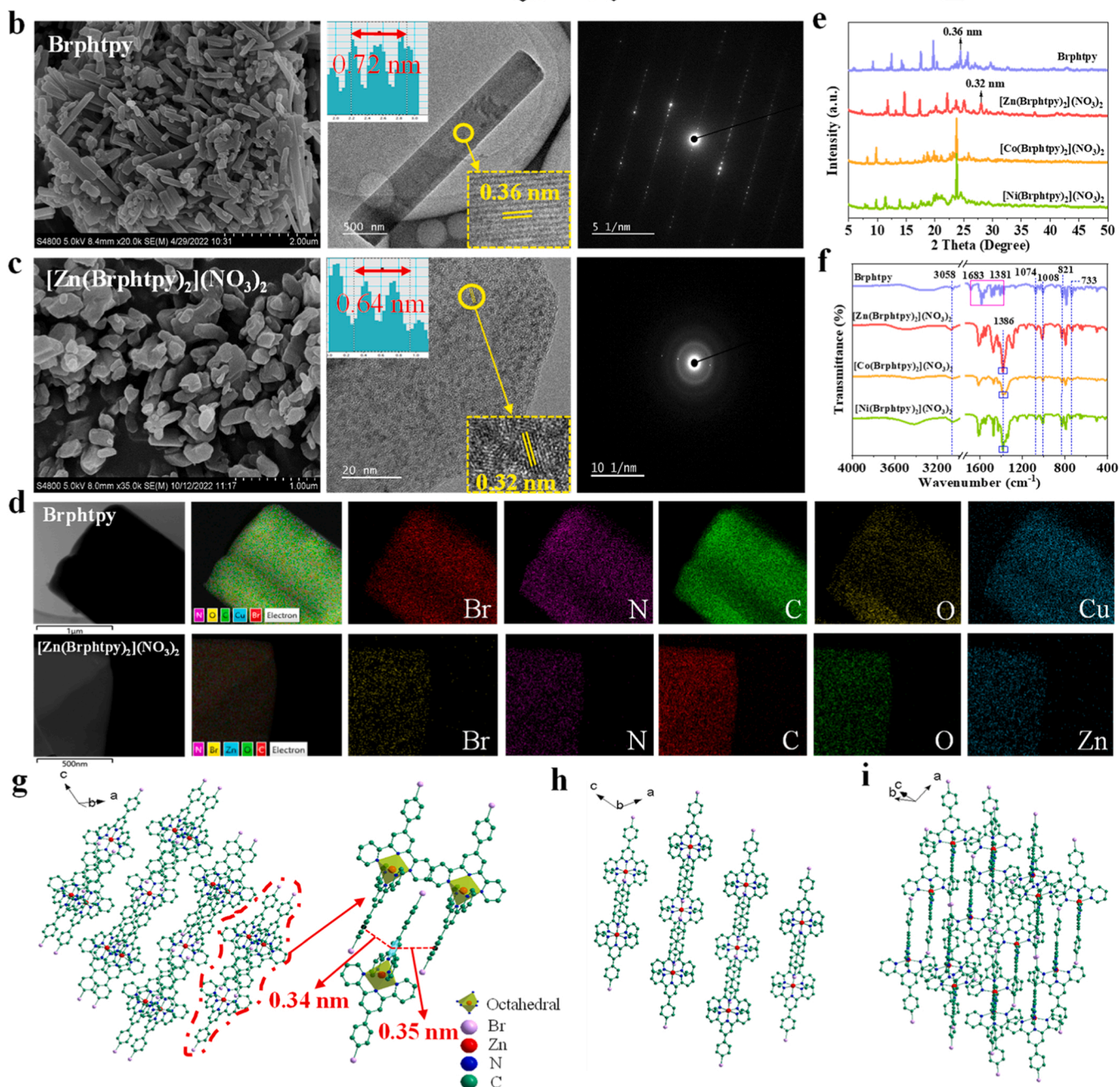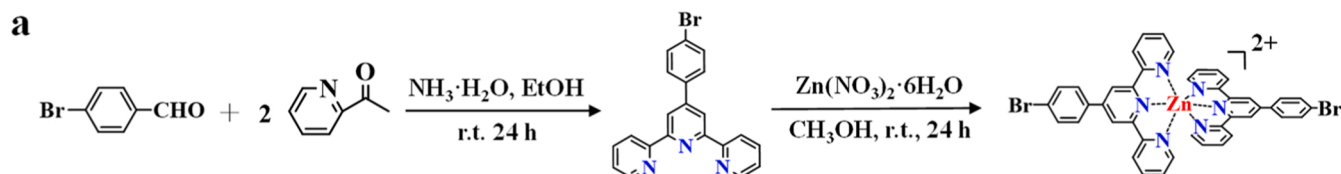
2.4. Photocatalytic activity tests

Photocatalytic reduction of CO_2 was carried out in gas-solid phase reactor system containing a stainless steel vessel (53 mL) equipped with petri dishes with top and bottom layers, and it was sealed with a quart plate that can pass through the irradiated light. This vessel was surrounded with cycling water to keep the reaction temperature of 25 °C. In order to obtain the uniform dispersion of the photocatalyst on the top layer of petri dishes, the aqueous suspension containing 7.5 mg of the photocatalyst was sonicated for 5 min, then the water was evaporated in vacuumed oven at 60 °C for 6 h. 2.5 mL of H_2O was added to the bottom layer of the quart petri dishes to provide the hydrogen resource [24]. Prior to the illumination, the reaction vessel was vacuumed and purged with purity CO_2 three times by the connecting tube in the vessel in order to remove the air completely. A 300 W Xe lamp (PLS-SXE300CUV, Beijing Bofeilai Tech. Co.) was used as the light source, and the distance between light source and the vessel was 20 cm. During the illumination, the 1 mL of gas was extracted by the micro-injector and immediately injected into the gas chromatography (GC-7900, Shanghai Tianmei Co. Ltd.) to analyze the component and amount of the gas, and the irradiation time was 3 h. The reaction setup used for photocatalytic reduction of CO_2 was shown in the Fig. S4, and the standard curve of CO volume (uL) *vs*. peak area of CO was shown in the Fig. S5.

2.5. Characterization

Fourier transform infrared spectroscopy (FTIR) of the samples was conducted on a Prestige-21 spectrometer (Shimadzu Co., Japan) in the range of 400 ∼ 4000 cm^{-1} with spectroscopic grade KBr as the reference sample. The morphological characterization was measured by S4800 scanning electron microscope (SEM) (Hitachi, Japan) at 10 kV, and JEM 2100-F transmission electron microscope (TEM) (JEOL, Ltd., Japan) at 200 kV. In addition, selected area electron diffraction (SAED) and energy dispersive X-ray spectroscopy (EDX) were also recorded using this

TEM. The TEM samples were prepared by the negative-staining method. A drop of dilute ethanol suspension of the sample was placed on a carbon-coated copper grid for 5 min. Next, the copper grid was put with one drop of uranyl acetate solution (0.5 wt%) for 5 min. Finally, the excess liquid was removed with filter paper, and the copper grid was dried at room temperature overnight. X-ray diffraction (XRD) analysis was performed on a Rigaku D/Max-2500 X-ray diffractometer (Rigaku Corporation, Japan) with Cu Kα radiation ($\lambda = 1.5406$ Å) at 40 kV and

100 mA. UV–vis diffuse reflectance spectroscopy (UV–vis DRS) was investigated by a Shimadzu-2550 Scan UV–vis system (Shimadzu, Japan) equipped with an integrating sphere attachment, and the measurement wavelength ranges from 200 to 800 nm with $BaSO_4$ as a reference. Steady-state photoluminescence (PL) spectra were recorded by an F-4600 FL fluorescence spectrophotometer (Hitachi Co., Japan) using a Xenon lamp as the excitation source, and the excitation wavelength was 275 nm. Time-resolved photoluminescence (TR-PL) spectra

Fig. 1. (a) Synthesis routes of Brphtpy and $[Zn(Brphtpy)_2](NO_3)_2$; (b-d) SEM, TEM images and SAED patterns of Brphtpy and $[Zn(Brphtpy)_2](NO_3)_2$; (e) XRD and (f) FTIR spectra of as-prepared samples; (g-i) Packing structure of $[Zn(Brphtpy)_2](NO_3)_2$ single crystal (red dashed lines represent π-π staking interactions).

were recorded on an F-4600 fluorescence spectrophotometer, and the fluorescence decay spectra were measured on an Edinburgh FLS980 fluorescence spectrophotometer (England, Edinburgh Instrument Co., Ltd.) and the excitation wavelength was 310 nm. ^{1}H Nuclear magnetic resonance spectra (^{1}H NMR) were recorded on an Avance 500 MHz spectrometer (Bruker Co., Germany). The high-resolution electrospray ionization mass spectroscopy (HR-ESI-MS) spectra were acquired from LCQ-TOFMS7000 mass spectrometer (Guangzhou Hexin Instrument Co., China). The electron paramagnetic resonance (EPR) spectra were measured on CIQTEK EPR200-Plus (Guoyi Quantum Technology Co., LTD, China) with continuous-wave X band frequency. Transient photo-current (TPC) and Mott-Schottky plots were collected on a standard three-electrode electrochemical analyzer (CH Instruments, China). The sample-coated ITO electrode was used as the working electrode, the saturated calomel electrode was taken as the reference electrode, and Pt net served as the counter electrode. 0.2 M Na$_2$SO$_4$ solution was employed as the electrolyte. The working electrode was prepared as follows: 5 mg sample and 2 mg polyethylene glycol were dispersed in 500 μL ethanol. Then, the suspension was uniformly dropped on 1.0 × 1.0 cm^2 ITO conductive glass until the rest was dried. Single crystal X-ray diffraction analysis (SC-XRD), including data collection, cell refinement, and data reduction, were collected on a Bruker PHOTONIII diffractometer with graphite-monochromatic Cu Ka radiation (λ = 1.54178 Å) at 173 K. The structure was solved by direct methods using SHELXT-2018, and all of the non-hydrogen atoms were refined aniso-tropically by full-matrix least-squares on F^2 using SHELXL-2018. Crystallographic data and structure refinement parameters were summarized in Table S2, and selected bond lengths were listed in Table S3. X-ray photoelectron spectroscopy (XPS) was measured at Thermo Fisher Scientific K-Alpha with Al Kα X-ray (hv = 1486.6 eV) irradiation. The X-ray anode was run at 250 W, and the high voltage was kept at 15.0 kV with a detection angle of 54°. Inductively coupled plasma optical emission spectroscopy (ICP-OES) was measured by Agilent 5110.

3. Results and discussion

Conjugated ligand Brphtpy was synthesized through the Kröhnke reaction between 2-acetylpyridine and 4-bromobenzaldehyde (Fig. 1a). Zn(NO$_3$)$_2$·6 H$_2$O, Co(NO$_3$)$_2$·6 H$_2$O and Ni(NO$_3$)$_2$·6 H$_2$O methanol solutions were added dropwise into Brphtpy dichloroethane solution under stirring, and the corresponding resulting product of [M(Brphtpy)$_2$](NO$_3$)$_2$ was obtained. The π-π stacking interactions between Brphtpy molecules were easily formed due to the rigid structure of terpyridine and benzene units of Brphtpy. The existence of π-π stacking interactions can be verified by the clear lattice spacing of 0.36 nm in HRTEM (Fig. 1b), which is a typical intermolecular π-π stacking distance. And, it corresponds to the sharp diffraction peak of 24.4° in the XRD patterns (Fig. 1e). Brphtpy molecules self-assemble to a regular rod-like structure with a length of submicron size and a width of hundreds of nanometers through the π-π stacking interactions, and it shows a single crystalline conformation seen from the bright spot pattern spectrum of Brphtpy [25]. The overlap of long-range delocalized π-electrons along the conjugated Brphtpy π aggregates endows their conductive property, and the conductivity is 4.94 S cm^{-1} determined by a four-point probe meter and which is in the semiconductor range.

[Zn(Brphtpy)$_2$](NO$_3$)$_2$ presents a stacked nanoparticles structure, and the average diameter of nanoparticles is hundreds of nanometers (Fig. 1c). The lattice spacing of 0.32 nm corresponds to the XRD diffraction peak of 28.1° (Fig. 1e) indicating that π-π stacking interactions still existed after the coordination with Zn^{2+}. As shown in the packing structure of [Zn(Brphtpy)$_2$](NO$_3$)$_2$ single crystal (Fig. 1g), the π-π interaction exists between the central pyridine ring and the adjacent molecules' benzene ring. The π-π stacking distances are 0.34 and 0.35 nm arising from the vertical distance between the plane of the pyridine ring to the center of neighbor molecules' benzene rings, which

are near to the lattice spacing of 0.32 nm. Extended π-π stacking interactions were formed along the *b* axis (Fig. S6). Moreover, the complex exhibits distorted tetrahedral structure and the coordinated number is six (Figs. 1g-1i). As shown in the Fig. 1g, Zn^{2+}-coordinated two Brphtpy ligands are vertical and aromatic rings of every ligand are almost coplanar, which is conductive to the transfer of electron to Zn^{2+}. The SAED pattern indicates that the samples are of polycrystalline nature [26]. The EDS mapping (Fig. 1d) of Brphtpy shows the presence of N, O, Br, C and Cu elements, suggesting that Brphtpy photocatalyst has been successfully synthesized. The Cu element originates from the Cu grid in the TEM sample preparation process. The uniform distribution of Zn and N elements in the Brphtpy further verified the successful coordination of Zn^{2+} ions with Brphtpy ligands.

In the FTIR spectra (Fig. 1f), the weak peak of 3058 cm^{-1} belongs to the stretching vibration of C-H in pyridine rings and benzene rings. The peaks of 1074, 1008 cm^{-1}, and the peaks in the range of 821 and 733 cm^{-1} are attributed to the out-of-plane and in-plane bending vibration of C-H bonds in benzene rings and pyridine rings, respectively. The peaks from 1381 to 1683 cm^{-1} for Brphtpy are assigned to the C=C and C=N stretching vibrations in benzene rings and pyridine rings. Notably, after the coordination of metal ions, C=C and C=N peaks are redshift, and the number of peaks decreases obviously because of the formation of coordinate bonds between pyridine rings and metal ions, and the electrons easily transfer from pyridine rings to metal ions which weaken C=C and C=N bonds of pyridine rings [27]. Moreover, a new peak at 1386 cm^{-1} appears assigning to the NO$_3^-$ ligands [28], further demonstrating the successful synthesis of [Zn(Brphtpy)$_2$](NO$_3$)$_2$, [Co(Brphtpy)$_2$](NO$_3$)$_2$ and [Ni(Brphtpy)$_2$](NO$_3$)$_2$ photocatalysts.

The molecular weights of the as-prepared complexes were characterized by positive ion mode HR-ESI-MS (Fig. 2a). The molecular ion peaks of *m/z* at 421.0, 417.5, 417.0 correspond to the double-charged molecular ion of species with measured molecular weights (Found) of 842.0, 835.0, 834.0. Given these complexes contain bis(terpyridine) ligands and the coordination number is six, the calculated molecular weights of [Zn(Brphtpy)$_2$]$^{2+}$, [Co(Brphtpy)$_2$]$^{2+}$ and [Ni(Brphtpy)$_2$]$^{2+}$ are 841, 835, 835, which are near to the found values. Based on this result, it can be deduced that these complexes are six-coordination structure and their chemical structures are shown in the inset figure of Fig. 2a. The six-coordination structure of [Zn(Brphtpy)$_2$](NO$_3$)$_2$ also was proved by the result of single crystal XRD diffraction (Fig. 1g). These hexacoordinated complexes possess octahedral geometry based on the crystal-field theory. In the octahedral geometry, the hybridized type is sp^{3}d^2 (Fig. S7) or d^{2}sp^3 (Fig. S8) between empty orbitals of central metal ion and the lone pair electrons of N atoms in terpyridine ligands according to the Valence Bond Theory. As shown in Fig. S7 and Fig. S8, the d^7, d^8 and d^{10} electrons of Co^{2+}, Ni^{2+} and Zn^{2+} occupy at least four d orbitals, so it can only provide at most one unoccupied 3d orbital to hybridize, thus the hybridization type is sp^{3}d^2 not the d^{2}sp^3. Accordingly, these complexes belong to outer orbital complexes and exhibit high spin states. The corresponding d-orbital electron configurations of Co^{2+}, Ni^{2+} and Zn^{2+} according to the Hund Rule and Pauli Exclusion Principle were shown in Fig. 2c. It can be seen that the d orbitals of Co^{2+} and Ni^{2+} contain unpaired d electrons, and Zn^{2+} are filled. The EPR peaks (Fig. 2b) of [Co(Brphtpy)$_2$](NO$_3$)$_2$ and [Ni(Brphtpy)$_2$](NO$_3$)$_2$ at G values at ~3500 are assigned to the unpaired d electrons of Co^{2+} and Ni^{2+}, whereas no single was discovered for [Zn(Brphtpy)$_2$](NO$_3$)$_2$ due to its full d orbital [29].

UV–vis DRS spectra were employed to investigate the ultraviolet-visible absorption behavior of the as-prepared catalysts. As illustrated in Fig. 2d, Brphtpy photocatalyst displays an ultraviolet absorption band between 200 and 350 nm assigned to the n-π * and π-π * transition of C=N and C=C groups of pyridine rings and benzene rings. The absorption band of [Zn(Brphtpy)$_2$](NO$_3$)$_2$ exhibits a redshift of ~10 nm compared to Brphtpy because coordination between zinc ion and N atoms of terpyridine with lone pair electrons enlarges the conjugated degree of this system, resulting in the decreased energies of π-π * and n-
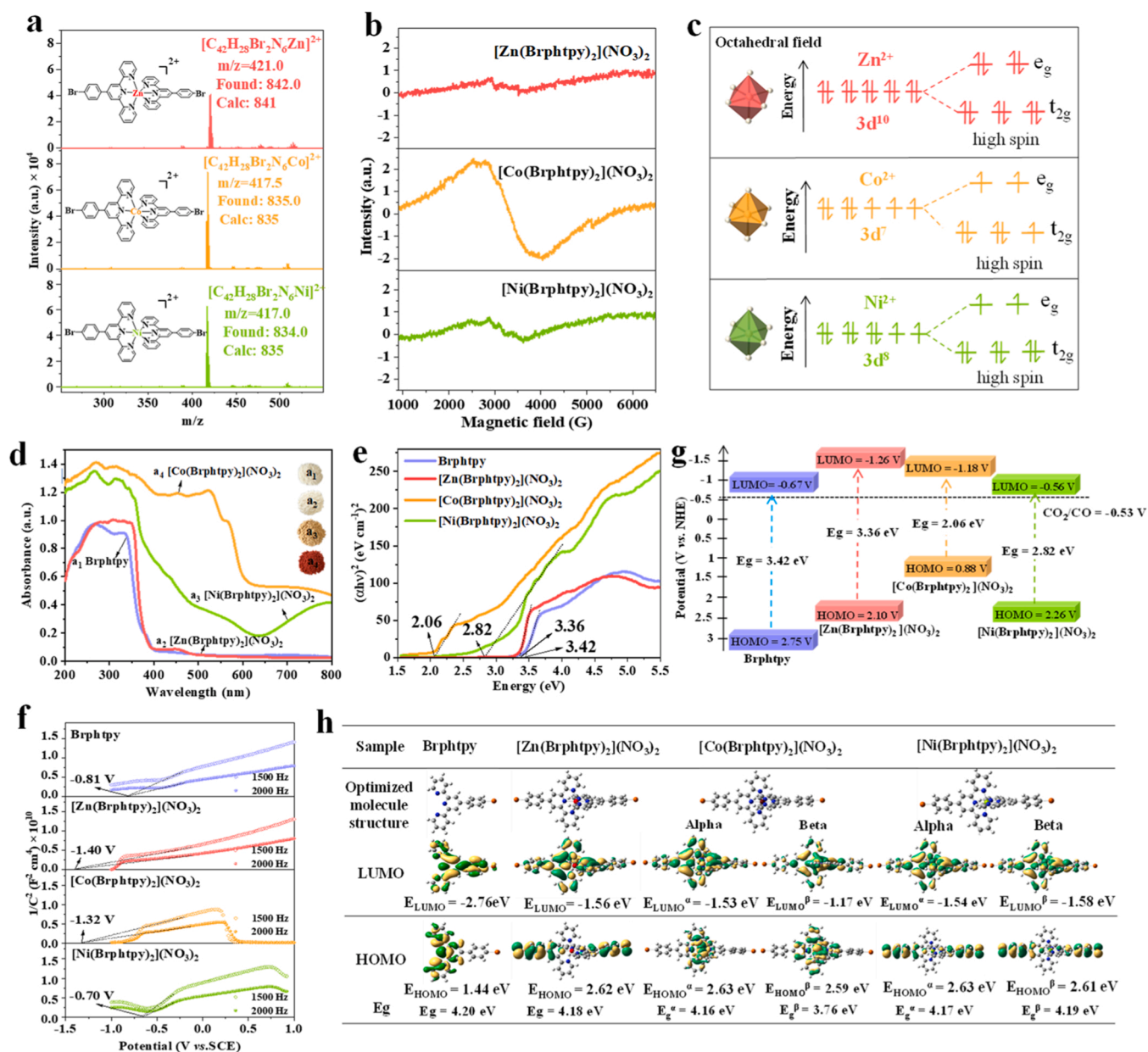
Fig. 2. (a) The HR-ESI-MS (b) EPR and (c) *d*-orbital electronic configurations of central metals (Zn^{2+}, Co^{2+} and Ni^{2+}) of [Zn(Brphtpy)$_2$](NO$_3$)$_2$, [Co(Brphtpy)$_2$](NO$_3$)$_2$ and [Ni(Brphtpy)$_2$](NO$_3$)$_2$; (d) UV–vis DRS spectra, (e) the Tauc polts and (f) Motto-Schottky plots and (g) energy structure and (h) frontier molecular orbital (FMOs) of as-prepared samples.

π^* transition and the occurrence of red-shift of light absorption. [Co(Brphtpy)$_2$](NO$_3$)$_2$ and [Ni(Brphtpy)$_2$](NO$_3$)$_2$ show remarkably expanded and significantly enhanced absorption band in the UV-Vis light region compared to [Zn(Brphtpy)$_2$](NO$_3$)$_2$, which was due to the *d-d* transitions wherein the electrons present in the ground state absorb light and jump into a higher energy level. Then, the complexes show the color of absorbing light's complementary color, such as the dark red of [Co(Brphtpy)$_2$](NO$_3$)$_2$ and the pale yellow of [Ni(Brphtpy)$_2$](NO$_3$)$_2$ (The inset optical photographs of Fig. 2d). However, [Zn(Brphtpy)$_2$](NO$_3$)$_2$ does not exist the *d-d* transitions because of the full-filled *d*-orbital and its appearance color is white [30].

Furthermore, the corresponding band gap (*Eg*) values of the prepared samples were evaluated by the Kuberlka-Munk (KM) method and were acquired by the Tauc plots (Fig. 2e), and, the *Eg* values of Brphtpy, [Zn(Brphtpy)$_2$](NO$_3$)$_2$, [Co(Brphtpy)$_2$](NO$_3$)$_2$ and [Ni(Brphtpy)$_2$](NO$_3$)$_2$ are approximately 3.42, 3.36, 2.06, 2.82 eV, respectively. The flat band

potential (*E*$_{fb}$) was measured by the extrapolation of the Mott-Schottky plots (Fig. 2f), and the positive slope of the curve demonstrates the n-type semiconductors characteristics of as-prepared photocatalysts[20]. In general, for n-type semiconductor, the CB (LUMO) is more negative about 0.1 V for flat-band potential, so the LUMO potentials of Brphtpy, [Zn(Brphtpy)$_2$](NO$_3$)$_2$, [Co(Brphtpy)$_2$](NO$_3$)$_2$, [Ni(Brphtpy)$_2$](NO$_3$)$_2$ photocatalysts are –0.91, –1.50, –1.42 and –0.80 V, respectively. When saturated calomel electrode (SCE) was used as a reference electrode, the LUMO was further transformed to –0.67, –1.26, –1.18, and –0.56 V *vs.* NHE based on the equation $E_{(LUMO\ vs.\ NHE)} = E_{SCE} + 0.24\ V$. The HOMO potentials of Brphtpy, [Zn(Brphtpy)$_2$](NO$_3$)$_2$, [Co(Brphtpy)$_2$](NO$_3$)$_2$ and [Ni(Brphtpy)$_2$](NO$_3$)$_2$ were determined to be 2.75, 2.10, 0.88 and 2.26 V, respectively, according to the equation of $E_{LUMO} = E_{HOMO} - E_g$. The detailed energy level structures of as-prepared samples are shown in Fig. 2g. The LUMO potentials of all samples are more negative than that of the standard redox potential of CO_2/CO (–0.53 V), which have a

theoretically feasible reduction of CO_2 to CO[31,32]. The most negative LUMO energy of $[Zn(Brphtpy)_2](NO_3)_2$ means the stronger CO_2 reduction ability.

The simulated frontier molecular orbitals (FMOs) and optimized structures of as-prepared samples were calculated by B3LYP/6–31 + G (d, p) (ub3lyp) method in Gaussian software and the results were shown in Fig. 2h. The HOMO orbital of Brphtpy molecule mostly locates on the terpyridine units, while the LUMO is concentrated on the whole molecules. Notably, the central pyridine ring is not coplanar with other pyridine rings and benzene rings, owing to the repulsive force of N atoms. Whereas, after the coordination of Zn^{2+} ions, the electron deficiency ability of Zn^{2+}-bis(terpyridine) section is stronger than the benzene-Br section though Br is a typical electron drawing group, which is in good consistence with the DFT calculated results that the HOMO mainly distributed on the benzene-Br section, and the LUMO is close to the terpyridine rings. HOMO and LUMO of $[Zn(Brphtpy)_2](NO_3)_2$ are concentrated on the ligand section nor central Zn^{2+} ion (Table S5), and separated HOMO and LUMO suggested that a strong intramolecular charge transfer (ICT) effect occurs owing to the enhanced withdrawing-electron ability from Zn^{2+}. ICT effect promotes the transfer and separation of photo-generated charges, and electrons easily transfer to the

LUMO which is close to the Zn^{2+}. This can be verified by the electrostatic potential distribution maps (Fig. S9). Blue and red maps represent positive and negative charge regions, respectively [33]. After introduction of Zn^{2+} to Brphtpy, the color of metallo-terpyridine region changed to blue, indicating that the Zn^{2+} reinforces the electron-deficient property of the terpyridine rings, and photogenerated electron easily directionally transfer toward Zn^{2+}. Meanwhile, Zn^{2+} is an absorption site of CO_2, then the photocatalytic CO_2 reduction reaction rapidly occurred. Different from the closed shell system of $[Zn(Brphtpy)_2](NO_3)_2$, $[Co(Brphtpy)_2](NO_3)_2$ and $[Ni(Brphtpy)_2](NO_3)_2$ contain the nonrestrictive open-shell transition metal cations due to the existence of single electron, and they contain two orbitals of alpha (α) and beta (β) orbitals arising from the spin up and spin down of single electron in the complex [34]. The α/β-HOMO and α/β-LUMO of $[Co(Brphtpy)_2](NO_3)_2$ are 2.63/2.59-HOMO eV (*vs.* NHE) and $-1.53/-1.17$ eV (*vs.* NHE). The α/β-HOMO and α/β-LUMO of $[Ni(Brphtpy)_2](NO_3)_2$ are 2.63/2.61-HOMO eV (*vs.* NHE) and $-1.54/-1.58$ eV (*vs.* NHE) (The relevant calculation as shown in Table S4), and it was notified that the HOMO and LUMO overlay in Co^{2+}-pyridine and Ni^{2+} section, respectively, and the magnified images as shown in Table S6 and Table S7. The overlap of the HOMO and LUMO
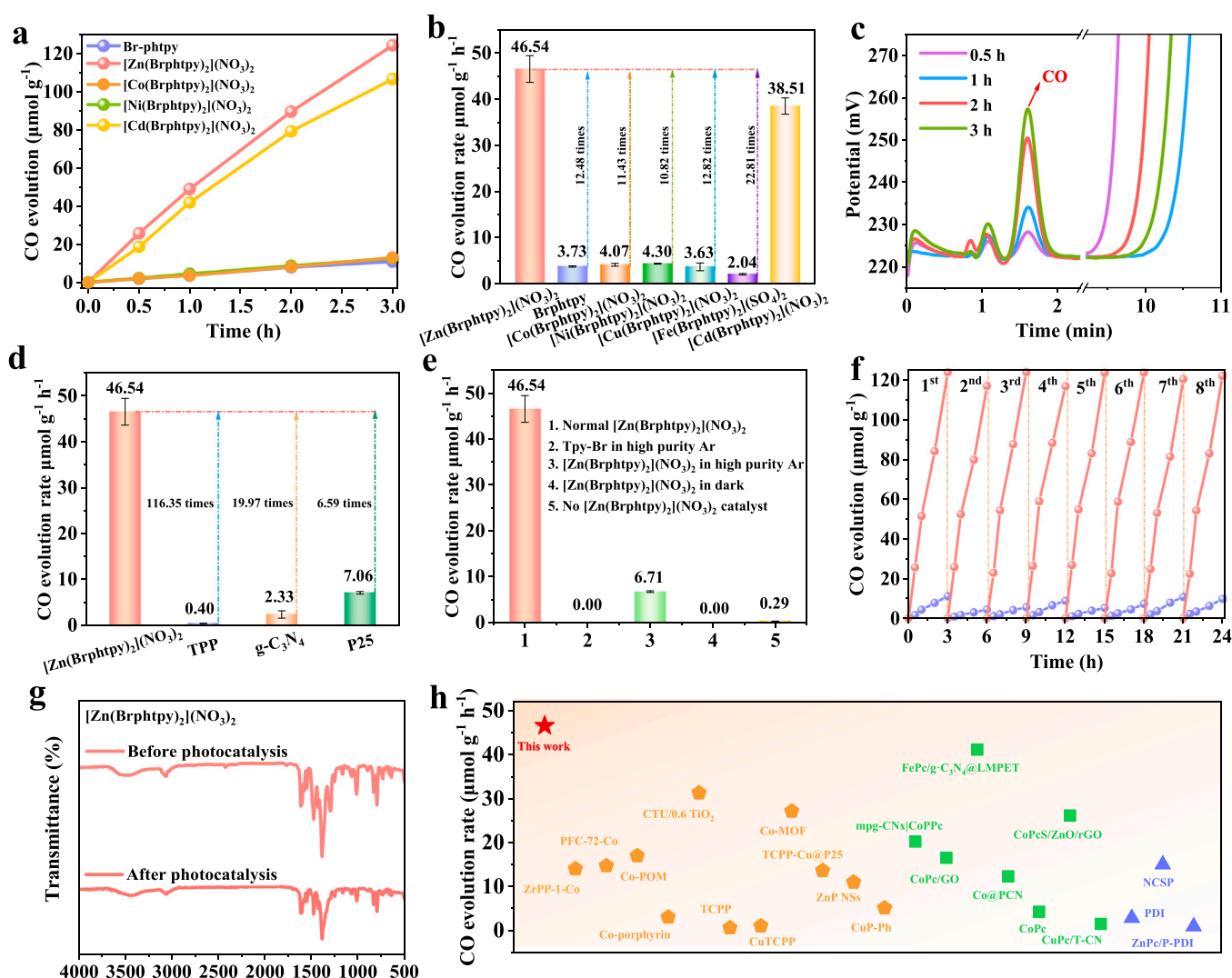

Fig. 3. (a) Time course of CO evolution amount and (b) CO evolution rates of as-prepared samples, and the error bars represent the standard deviation of four independent experiment measurements (the photocatalytic CO_2 reaction at 0.5, 1, 2 and 3 h); (c) The peak area of CO produced by $[Zn(Brphtpy)_2](NO_3)_2$ with irradiation time increasing; (e) CO evolution rates of $[Zn(Brphtpy)_2](NO_3)_2$ under different reaction conditions; (f) Cyclic stability test of Brphtpy and $[Zn(Brphtpy)_2](NO_3)_2$ for photocatalytic CO_2 reduction; (g) The FTIR spectra of $[Zn(Brphtpy)_2](NO_3)_2$ before and after photocatalytic reduction of CO_2; Comparison photocatalytic CO_2 reduction activity of $[Zn(Brphtpy)_2](NO_3)_2$ with (d) common photocatalysts and (h) reported supramolecular photocatalysts.

is unfavorable for charge separation, leading to low photocatalytic CO_2 reduction activity. Additionally, the calculated HOMO and LUMO energies of as-prepared samples are different from measured values because calculated molecule is isolated molecule which possesses discrete HOMO and LUMO levels, whereas the HOMO and LUMO of self-assembled photocatalyst are similar to the band-like electronic structure of inorganic semiconductor based on the intermolecular transfer integrals of HOMOs and LUMOs [35]. This above reason leads to the fact that the calculated energy gaps of as-prepared samples (4.20 eV of Brphtpy, 4.18 eV of [Zn(Brphtpy)$_2$](NO$_3$)$_2$, 4.16 and 3.76 eV for α/β orbital of [Co(Brphtpy)$_2$](NO$_3$)$_2$, 4.17 and 4.19 eV for α/β orbital of [Ni(Brphtpy)$_2$](NO$_3$)$_2$) are obviously larger than the experimental values (3.42 eV of Brphtpy, 3.36 eV of [Zn(Brphtpy)$_2$](NO$_3$)$_2$, 2.06 eV of [Co(Brphtpy)$_2$](NO$_3$)$_2$, 2.82 eV of [Ni(Brphtpy)$_2$](NO$_3$)$_2$).

The photocatalytic CO_2 reduction performance of the as-prepared samples was investigated in a solid-gas phase reactor system with H_2O vapor, and without sacrificial agent and photosensitizer. As shown in Fig. 3a, the CO evolution amounts of as-prepared samples increased with time increasing. The average photocatalytic CO evolution rate of [Zn(Brphtpy)$_2$](NO$_3$)$_2$ within 3 h is 46.54 µmol g^{-1} h^{-1}(Table S1), which is 12.48 times higher than Brphtpy photocatalyst. This was because, after the introduction of Zn^{2+}, strong ICT effect facilitates electron transfer from donor bromo-phenyl to acceptor terpyridine, thus promoting efficient separation of electrons and holes, allowing more electrons to participate in the photocatalytic CO_2 reaction. Isotope-labeled carbon dioxide ($^{13}CO_2$) instead of CO_2 was carried out to investigate whether the CO origin from the input CO_2. As shown in the Fig. S10, the MS signal at $m/z = 29$ belongs to ^{13}CO, confirming that the produced CO exactly originated from the CO_2 using [Zn(Brphtpy)$_2$](NO$_3$)$_2$ as photocatalysts [36]. [Co(Brphtpy)$_2$](NO$_3$)$_2$ and [Ni(Brphtpy)$_2$](NO$_3$)$_2$ exhibit low CO evolution rates of 4.07 and 4.30 µmol g^{-1} h^{-1} (Fig. 3b), which was due to the fact that the photogenerated electrons transferred from the excited bis(terpyridine) to Co^{2+} and Ni^{2+}, resulting in the nonradiative deactivation of photoexcited electrons, which is not benefit to the photocatalytic CO_2 reduction reaction. To further illustrate that the d-orbital electron affects the photocatalytic activity, the outmost d^{10}, d^9 and d^6 electron configurations of Cd^{2+}, Cu^{2+} and Fe^{2+} were chosen as the central metal ions to prepare the photocatalysts, and the CO evolution rates are 38.51, 3.63 and 2.04 µmol g^{-1} h^{-1}, respectively, also indicating the d-orbital electron configuration is the main reason to tune the photocatalytic activity.

Moreover, [Zn(Brphtpy)$_2$](NO$_3$)$_2$ exhibits a significantly higher CO evolution rate than that of the common photocatalysts such as P25, C_3N_4, TPP (Fig. 3d). The photocatalytic activity of Brphtpy was investigated by the replace of CO_2 by Ar gas, and without CO was detected, suggesting that CO indeed originated from the filled CO_2 rather than catalysts. Moreover, a small amount of CO was detected when [Zn(Brphtpy)$_2$](NO$_3$)$_2$ as photocatalyst filled with Ar gas, which may be arising from the reduction of adsorbed CO_2 on the catalyst surface because [Zn(Brphtpy)$_2$](NO$_3$)$_2$ has a strong affinity towards CO_2 by the coordination interaction between O and Zn^{2+}. Additionally, the controlling tests were carried out under the conditions of dark and no photocatalyst. No CO was produced under dark conditions, indicating that the generated CO was from the photocatalytic process. A negligible CO amount of 0.29 µmol g^{-1} h^{-1} is generated in the absence of catalyst (Fig. 3e). The cyclic experiments showed (Fig. 3f) that the CO evolution amounts of the Brphtpy and [Zn(Brphtpy)$_2$](NO$_3$)$_2$ supramolecular photocatalysts still retained after eight consecutive runs for 24 h, indicating that the two samples had good photocatalytic stability. Additionally, the FTIR spectra (Fig. 3g and Fig. S12), SEM and TEM images (Fig. S11) and HR-ESI-MS spectra (Fig. S13) of as-prepared samples were barely changed after photocatalysis, which further confirms the excellent photocatalytic stability of the samples. Fig. 3h exhibits that the photocatalytic CO evolution performance of [Zn(Brphtpy)$_2$](NO$_3$)$_2$ is better than that of some reported supramolecular photocatalysts (the specified experimental conditions and relevant information as shown in

Table S8), for example, porphyrin-based compound and their derivatives (orange pentagon), phthalocyanine and their derivatives (green quadrangle), and, perylene diimide and their derivatives (blue triangle).

The steady-state PL spectra of as-prepared photocatalysts were performed to study the transfer behavior of photogenerated electrons and were determined using 275 nm as excitation wavelength. As shown in Fig. 4a, Brphtpy exhibits a PL emission peak at 378 nm due to the n-π * and π-π * transitions of C≡N groups of pyridine rings and C≡C groups of the benzene ring. No fluorescence of [Co(Brphtpy)$_2$](NO$_3$)$_2$ and [Ni(Brphtpy)$_2$](NO$_3$)$_2$ was observed due to the ligand-to-metal charge transfer (LMCT) effect through the rapid transfer of photogenerated electrons generated by the excited bis(terpyridine) ligand to the unfilled orbitals of paramagnetic Co^{2+} and Ni^{2+} ions (d^7 and d^8 configuration, respectively), which involved in an energy-transfer mechanism, leading to the nonradiative PL quenching. LMCT gives rise to the nonradiative deactivation of photoexcited electrons, which is unfavorable for photocatalytic CO_2 reduction. Whereas the enhancement fluorescence of [Zn(Brphtpy)$_2$](NO$_3$)$_2$ is due to the filled stable d^{10} electronic configuration of Zn^{2+}, which does not participate in such electron-transfer process to deactivate the excited states, and the formation of a rigid system after binding with Zn^{2+}, leads to chelation-enhanced fluorescence [37]. From another point of view, the stronger PL intensity also suggests that higher photogenerated electron concentration per unit volume, thus, as for [Zn(Brphtpy)$_2$](NO$_3$)$_2$, more excited state electrons are available for photocatalytic CO_2 reduction. The PL lifetime of the photoexcited carriers was investigated by time-resolved PL spectroscopy (Fig. 4b), and the average lifetime (τ$_{avg}$) could be calculated according to the following equation:

$$\tau_{avg} = \frac{A_1\tau_1^2 + A_2\tau_2^2 + A_3\tau_3^2}{A_1\tau_1 + A_2\tau_2 + A_3\tau_3}$$

Where τ_1, τ_2 and τ_3 are the emission PL lifetimes, and A_1, A_2 and A_3 are the corresponding percentages of τ_1, τ_2 and τ_3, respectively. The relevant values and calculated process were shown in Table S9. Clearly, the calculated τ$_{avg}$ of Brphtpy, [Zn(Brphtpy)$_2$](NO$_3$)$_2$ are 5.89 and 0.70 ns, respectively. The shorter PL lifetime of [Zn(Brphtpy)$_2$](NO$_3$)$_2$ compared to Brphtpy is own to the faster interfacial electron transport from the benzene-Br section to the Zn^{2+}-bis(terpyridine) section. This result demonstrated that the electron transfer and separation efficiency improve after the introduction of Zn^{2+}. [Co(Brphtpy)$_2$](NO$_3$)$_2$, and [Ni(Brphtpy)$_2$](NO$_3$)$_2$ photocatalysts possess extremely short fluorescence lifetime when the excitation wavelength is 410 nm and it almost overlaps with the light source spectra owing to the fact the open-shell transition metal cations of Co^{2+} and Ni^{2+} produce LMCT state that is short-lived thermally activated decay [38]. LMCT process also leads to the decreased available photogenerated charges, which can be reflected in the low transient photocurrent of [Co(Brphtpy)$_2$](NO$_3$)$_2$ (0.035 uA cm^{-2}) and of [Ni(Brphtpy)$_2$](NO$_3$)$_2$ (0.017 uA cm^{-2}). [Zn(Brphtpy)$_2$](NO$_3$)$_2$ exhibits a stronger transient photocurrent (1.264 uA cm^{-2}) than Brphtpy photocatalyst (0.013 uA cm^{-2}) (Fig. 4c), suggesting that the increased available photo-generated charges generated by the ICT effect. Moreover, the smallest EIS Nyquist plot semicircle of [Zn(Brphtpy)$_2$](NO$_3$)$_2$ (Fig. S14), indicates the lowest charge transfer resistance of [Zn(Brphtpy)$_2$](NO$_3$)$_2$, facilitating the faster migration of the photogenerated electrons towards Zn^{2+} and reduce the absorbed CO_2 molecules.

To obtain more information on the electron transfer of the prepared photocatalysts, XPS characterizations were measured (Fig. 4d-f). The Zn 2p XPS spectrum for [Zn(Brphtpy)$_2$](NO$_3$)$_2$ shows two peaks at 1021.5 and 1044.5 eV corresponding to Zn 2p$_{1/2}$ and Zn 2p$_{3/2}$ respectively. The distance between the two peaks was determined to be 23.0 eV, attributing to the Zn^{2+} ions [39]. After the light illustration, there is no obvious change of the XPS spectrum of [Zn(Brphtpy)$_2$](NO$_3$)$_2$, suggesting that LMCT does not occur. The high-resolution Co 2p XPS
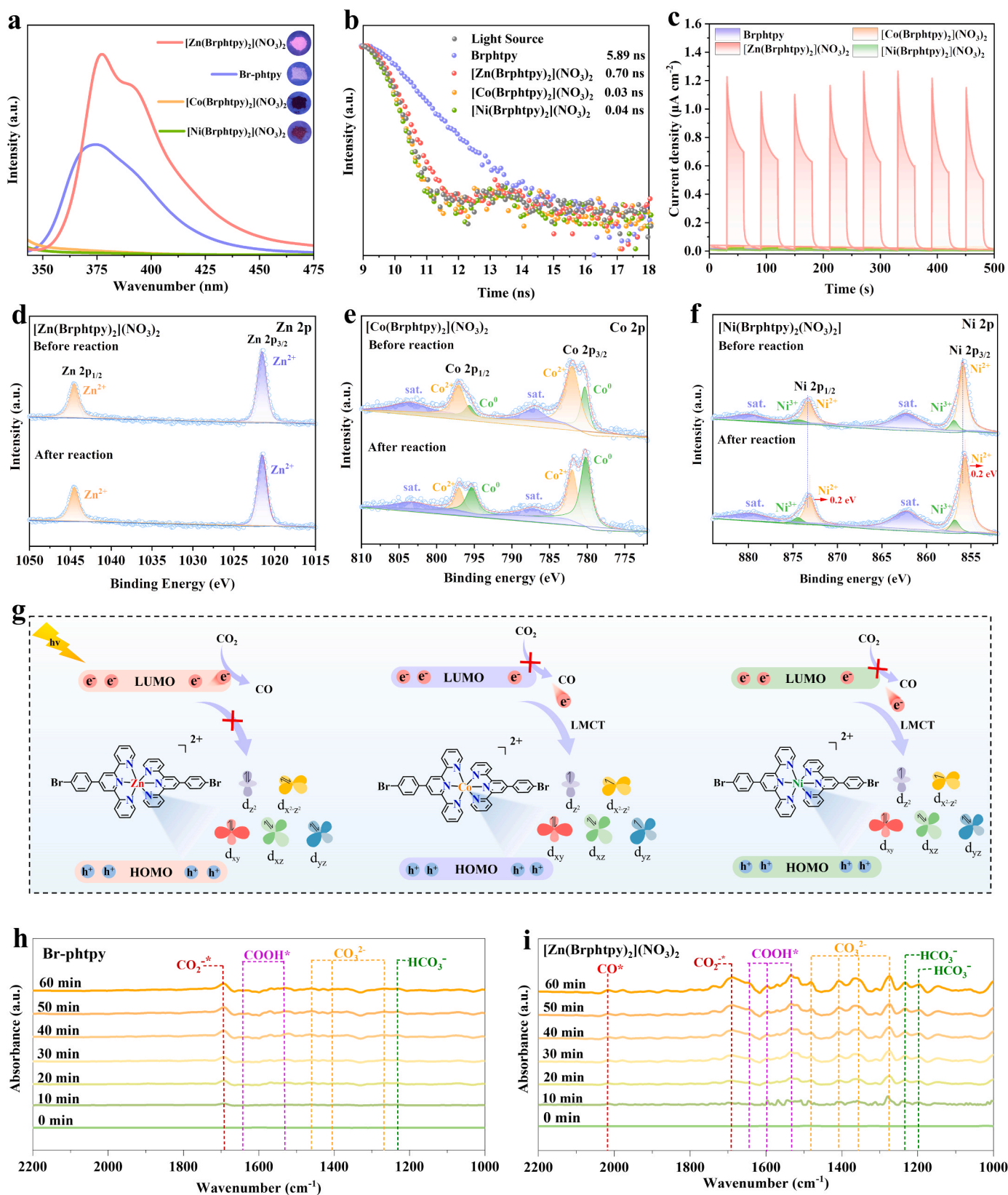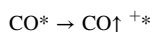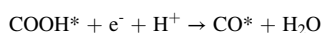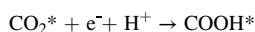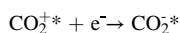
Fig. 4. (a) Steady-state PL spectra, (b) Time-resolved PL spectra, (c) Transient photocurrent (TPC) spectra of as-prepared photocatalysts; (d-f) High-resolution XPS spectra of $[Zn(Brphtpy)_2](NO_3)_2$, $[Co(Brphtpy)_2](NO_3)_2$ and $[Ni(Brphtpy)_2](NO_3)_2$; (g) The schematic representation of photocatalytic CO_2 reduction mechanism; (h-i) In situ FTIR spectra of Brphtpy, and $[Zn(Brphtpy)_2](NO_3)_2$ photocatalysts.

spectrum for $[Co(Brphtpy)_2](NO_3)_2$ can be deconvolved into four characteristic peaks of Co^{2+} (782.0 and 797.1 eV) and Co^0 (780.4 and 795.6 eV) along with two satellite (Sat.) peaks at 787.1 eV and 803.7 eV. After the illumination, the increased Co^0 was observed because more Co^{2+} was reduced to Co^0 through LMCT process, indicating the nonradiative deactivation of photo-excited electrons which were used for reduction of Co^{2+} instead of CO_2 reduction. The Ni $2p_{1/2}$ and Ni $2p_{3/2}$ peaks can be deconvolved into four characteristic peaks of Ni^{3+} (856.8 and 874.4 eV) and Ni^{2+} (855.8 and 873.2 eV). After the illumination, the binding energy values of Ni^{2+} decreased by 0.2 eV, demonstrating that the Ni^{2+} gains electrons by the LMCT process. Too small amount of Ni^0 to be observed but Co^0 can be observed because $Co(Brphtpy)_2(NO_3)_2$ has three unpaired electrons in $3d$ orbitals which is easier to get electrons than that of $Ni(Brphtpy)_2(NO_3)_2$ with two unpaired electrons in $3d$ orbitals through LMCT effect. Moreover, the existence of a small amount of Ni^{3+} may be from the NiOOH or Ni_2O_3 on the surface of $[Ni(Brphtpy)_2](NO_3)_2$ since Ni^{2+} was easily oxidized inevitably [40]. The schematic representation of photocatalytic CO_2 reduction mechanism was shown in Fig. 4g.

The emerging surface adsorbents and reaction intermediates of as-prepared samples in the photocatalytic CO_2 reduction process were investigated by the *in-situ* Fourier transform infrared spectroscopy (DR-FTIR). In the CO_2 adsorption process at dark (Fig. S15 and S16), the peaks at 2376, 2342, 2311 cm^{-1} are assigned to the asymmetric stretching of adsorbed CO_2 [41]. The peak of Brphtpy at 1650 and two peaks of $[Zn(Brphtpy)_2](NO_3)_2$ at 1547 and 1490 cm^{-1} correspond to the bidentate carbonate (b-CO_3^{2-}), and monodentate carbonate(m-CO_3^{2-}), bicarbonate (HCO$^-$), respectively. These peaks are caused by the transformation of a fraction of CO_2 to CO_3^{2-} or HCO$^-$ in the presence of H_2O molecules [42]. The peak intensity gradually increases with time increasing, indicating the successful adsorption of more CO and H_2O molecules on the surface of as-prepared photocatalysts. As depicted in Fig. 4h-i, several new peaks gradually appeared after light irradiation. The generated CO_2 * at 1694 cm^{-1} implies activation of CO_2 through the route of $CO_2 + e^- \rightarrow CO_2^-$* [43]. The peak of CO_2* on the surface of $[Zn(Brphtpy)_2](NO_3)_2$ was changed more significantly than that on the Brphtpy, indicating that $[Zn(Brphtpy)_2](NO_3)_2$ exhibits stronger capture of CO_2 than Brphtpy. The peaks appeared at 1644, 1534 and 2105 cm^{-1} are assigned to the COOH* and CO* , which are the most crucial intermediate in the photoreduction process of CO_2 to CO. The generation of COOH* is the rate-limiting step of the reaction, and CO* is the crucial intermediate for the formation of the final product CO [43]. Based on the above intermediate product, in the presence of H_2O, the process of reducing CO_2 to CO can be summarized as the following steps,

$$CO_2^+* + e^- \rightarrow CO_2^-*$$

$$CO_2^-* + e^- + H^+ \rightarrow COOH*$$

$$COOH* + e^- + H^+ \rightarrow CO* + H_2O$$

$$CO* \rightarrow CO\uparrow ^+*$$

Where * represent the surface active sites on the catalyst surface. Additionally, one electron reduces intermediate of C(=O)OCO_2 to C(=O)OCO_2^- which is more stable than CO_2^-, subsequently, one electron further reduces C(=O)OCO_2^- to carbonate (CO_3^{2-*}) and CO (C(=O)$OCO_2^- + e^- \rightarrow CO_3^{2-*} +$ CO), thus, CO_3^{2-*} peak can be observed [44]. In this process, CO_3^{2-*} is protonated by the H_2O, then the HCO_3^* can be observed in this spectrum. It was noteworthy that the crucial intermediates of COOH* and CO* were generated more quickly on $[Zn(Brphtpy)_2](NO_3)_2$ than that of Brphtpy indicating the formation of more intermediates and conversion to more CO on the surface of $[Zn(Brphtpy)_2](NO_3)_2$.

4. Conclusion

In summary, a series of photocatalysts were constructed by self-assembly of terpyridine-based molecules and non-noble metals (Zn^{2+}, Co^{2+}, Ni^{2+} and Cd^{2+}) through coordination interactions and π-π stacking interactions. The relationship between d electron configurations of central metals and photocatalytic CO_2 reduction activity was investigated. MS, EPR results combined with the crystal-field theory show the existence of unpaired electrons in the $3d$ orbitals of Co^{2+} and Ni^{2+}, whereas Zn^{2+} and Cd^{2+} with full electrons. PL, TPC and XPS results verified that the unpaired electrons of Co^{2+}, Ni^{2+} produce a ligand-metal charge transfer (LMCT) effect resulting in the nonradiative deactivation of photoexcited electrons which cannot be used for CO_2 reduction. Whereas, the Zn^{2+} and Cd^{2+} with filled d^{10} configuration do not occur LMCT, and improve the CO evolution rate to 46.54 and 38.51 μmol g^{-1} h^{-1} which is far higher than that of $[Co(Brphtpy)_2](NO_3)_2$ and $[Ni(Brphtpy)_2](NO_3)_2$. This work deeply investigates the relationship between the metal and activity, which is significant for the rational design and preparation of metallo-supramolecular photocatalysts with excellent photocatalytic activity.

CRediT authorship contribution statement

Jia Song: Investigation, Data curation, Visualization, Sample characterization. **Shanchao Wang:** Sample characterization. **Lin Wang:** Data curation, Writing – original draft, Conceptualization, Supervision. **Qingzhi Luo:** Supervision. **Jing An:** Modification. **Yandong Duan:** Calculation. **Desong Wang:** Project administration, Funding acquisition, Supervision, Writing – review & editing.

Declaration of Competing Interest

The authors declare that they have no known competing financial interests or personal relationships that could have appeared to influence the work reported in this paper.

Data availability

Data will be made available on request.

Acknowledgements

Appendix A. Supporting information

Supplementary data associated with this article can be found in the online version at doi:10.1016/j.apcatb.2023.123582.

References

[1] Z. Li, J. Liu, R. Shi, G.I. Waterhouse, X.D. Wen, T. Zhang, Fe-based catalysts for the direct photohydrogenation of CO_2 to value-added hydrocarbons, Adv. Energy Mater. 11 (2021), 2002783.

[2] Y. Fang, T. Liu, L. Chen, D. Chao, Exploiting consecutive photoinduced electron transfer (ConPET) in CO 2 photoreduction, Chem. Commun. 58 (2022) 7972–7975.

[3] Y. Li, X. Zhang, D. Liu, Recent developments of perylene diimide (PDI) supramolecular photocatalysts: a review, J. Photochem. Photobiol. C Photochem. Rev. 48 (2021), 100436.

[4] R. Sun, H. Yin, Z. Zhang, Y. Wang, T. Liang, S. Zhang, L. Jing, Graphene-modulated PDI/g-C3N4 all-organic S-scheme heterojunction photocatalysts for efficient CO_2 reduction under full-spectrum irradiation, J. Phys. Chem. C 125 (2021) 23830–23839.

[5] Z. Zhang, Y. Zhu, X. Chen, H. Zhang, J. Wang, A full-spectrum metal-free porphyrin supramolecular photocatalyst for dual functions of highly efficient hydrogen and oxygen evolution, Adv. Mater. 31 (2019), 1806626.

[6] X. Chu, Y. Qu, A. Zada, L. Bai, Z. Li, F. Yang, L. Zhao, G. Zhang, X. Sun, Z.D. Yang, Ultrathin phosphate-modulated Co phthalocyanine/g-C3N4 heterojunction photocatalysts with single Co–N4 (II) sites for efficient O2 activation, Adv. Science 7 (2020), 2001543.

[7] J. Yang, J. Jing, Y. Zhu, A. Full-Spectrum, Porphyrin–fullerene D–A supramolecular photocatalyst with giant built-in electric field for efficient hydrogen production, Adv. Mater. 33 (2021) 2101026.

[8] A.M. Cancelliere, F. Puntoriero, S. Serroni, S. Campagna, Y. Tamaki, D. Saito, O. Ishitani, Efficient trinuclear Ru (ii)–Re (i) supramolecular photocatalysts for CO 2 reduction based on a new tris-chelating bridging ligand built around a central aromatic ring, Chem. Sci., 11 (2020) 1556–1563.

[9] Y. Wang, T. Liu, L. Chen, D. Chao, Water-assisted highly efficient photocatalytic reduction of CO2 to CO with noble metal-free bis (terpyridine) iron (II) complexes and an organic photosensitizer, Inorg. Chem. 60 (2021) 5590–5597.

[10] D. Gu, Y. Liu, X. Li, H. Zhu, Y. Cui, W. Yang, J. Hao, Porphyrin-based metal–organic frameworks loaded with Ag nanoparticles and their nanofibrous filters for the photocatalytic reduction of Cr (VI), Appl. Surf. Sci. 614 (2023), 156192.

[11] Y. Wang, Z. Zhao, R. Sun, J. Bian, Z. Zhang, L. Jing, TiO2-modulated tetra (4-carboxyphenyl) porphyrin/perylene diimide organic Z-scheme nano-heterojunctions for efficient visible-light catalytic CO2 reduction, Nanoscale 14 (2022) 8041–8049.

[12] Y. Guo, Q. Zhou, J. Nan, W. Shi, F. Cui, Y. Zhu, Perylenetetracarboxylic acid nanosheets with internal electric fields and anisotropic charge migration for photocatalytic hydrogen evolution, Nat. Commun. 13 (2022) 2067.

[13] R. Sun, Y. Wang, Z. Zhang, Y. Qu, Z. Li, B. Li, H. Wu, X. Hua, S. Zhang, F. Zhang, L. Jing, Ultrathin phosphate-modulated zinc phthalocyanine/perylenete diimide supermolecule Z-scheme heterojunctions as efficiently wide visible-light photocatalysts for CO2 conversion, Chem. Eng. J. 426 (2021), 131266.

[14] P. Verma, A. Singh, F.A. Rahimi, T.K. Maji, Colocalization of light harvesting and catalytic units in a 'soft' coordination polymer hydrogel toward visible-light driven photocatalytic hydrogen production, J. Mater. Chem. A 9 (2021) 13608–13614.

[15] Z. Gao, Z. Li, Z. Gao, F. Wang, Supramolecular alternate donor–acceptor copolymers mediated by Pt··· Pt metal–metal interactions and their photocatalytic applications, Nanoscale 10 (2018) 14005–14011.

[16] L. Wang, X. Liu, L. Ji, Q. Luo, Y. Duan, J. An, X. Chen, Y. Zhang, J. Ren, D. Wang, Resin with short-range π-π stacking aggregates for an efficient photocatalyst, Chem. Eng. J. 433 (2022), 134502.

[17] L. Chen, T. Liu, D. Chao, Organic terpyridine molecule as an efficient cocatalyst for metal–free CO2 photoreduction mediated by mesoporous graphitic carbon nitride, Chem. Eng. J. 429 (2022), 132348.

[18] E. Lam, E. Reisner, A TiO2–Co (terpyridine) 2 photocatalyst for the selective oxidation of cellulose to formate coupled to the reduction of CO2 to syngas, Angew. Chem. 133 (2021) 23494–23500.

[19] X.-Y. Zhang, C.-F. Xie, S.-Q. Wang, X.-M. Cheng, Y. Zhang, Y. Zhao, Y. Lu, W.-Y. Sun, Coordination polymers with 2, 2′: 6′, 2″-terpyridine earth-abundant metal complex units for selective CO2 photoreduction, Inorg. Chem. 61 (2022) 1590–1596.

[20] P. Verma, F.A. Rahimi, D. Samanta, A. Kundu, J. Dasgupta, T.K. Maji, Visible-light-driven photocatalytic CO2 reduction to CO/CH4 using a metal–organic "Soft" coordination polymer gel, Angew. Chem. 134 (2022), e202116094.

[21] Z. Li, R. Shi, J. Zhao, T. Zhang, Ni-based catalysts derived from layered-double-hydroxide nanosheets for efficient photothermal CO 2 reduction under flow-type system, Nano Res. 14 (2021) 4828–4832.

[22] D. Samanta, M. Kumar, S. Singh, P. Verma, K.K. Kar, T.K. Maji, M.K. Ghorai, Triphenylamine and terpyridine–zinc (ii) complex based donor–acceptor soft hybrid as a visible light-driven hydrogen evolution photocatalyst, J. Mater. Chem. A 8 (2020) 21968–21972.

[23] P. Verma, A. Singh, F.A. Rahimi, P. Sarkar, S. Nath, S.K. Pati, T.K. Maji, Charge-transfer regulated visible light driven photocatalytic H2 production and CO2 reduction in tetrathiafulvalene based coordination polymer gel, Nat. Commun. 12 (2021) 7313.

[24] J. Xu, Z. Ju, W. Zhang, Y. Pan, J. Zhu, J. Mao, X. Zheng, H. Fu, M. Yuan, H. Chen, R. Li, Efficient infrared-light-driven CO2 reduction over ultrathin metallic Ni-doped CoS2 nanosheets, Angew Chem. 60 (2021) 8705–8709.

[25] A. Sadeghzadeh-Attar, Structural and optical characteristic of single crystal rutile-titania nanowire arrays prepared in alumina membranes, Mater. Chem. Phys. 182 (2016) 148–154.

[26] V. Madurai Ramakrishnan, M. Natarajan, S. Pitchaiya, A. Santhanam, D. Velauthapillai, A. Pugazhendhi, Microwave assisted solvothermal synthesis of quasi cubic F doped TiO2 nanostructures and its performance as dye sensitized solar cell photoanode, Int. J. Energy Res. 45 (2021) 17259–17268.

[27] X. Ma, J. Zhang, N. Tang, J. Wu, A thermo-responsive supramolecular organogel: dual luminescence properties and luminescence conversion induced by Cd 2, Dalton Trans. 43 (2014) 17236–17239.

[28] V.D. Singh, R.S. Singh, R.P. Paitandi, B.K. Dwivedi, B. Maiti, D.S. Pandey, Solvent-dependent self-assembly and aggregation-induced emission in Zn (II) complexes containing phenothiazine-based terpyridine ligand and its efficacy in pyrophosphate sensing, The, J. Phys. Chem. C 122 (2018) 5178–5187.

[29] J. Wang, Y.-C. Huang, Y. Wang, H. Deng, Y. Shi, D. Wei, M. Li, C.-L. Dong, H. Jin, S. S. Mao, Atomically dispersed metal–nitrogen–carbon catalysts with d-orbital electronic configuration-dependent selectivity for electrochemical CO2-to-CO reduction, ACS Catal. 13 (2023) 2374–2385.

[30] K.J. Al-Adilee, A. Shaimaa, Synthesis and spectral properties studies of novel hetrocyclic mono azo dye derived from thiazole and pyridine with some transition complexes, OJC 33 (2017) 1–14.

[31] S. Zhao, Q. Liang, Z. Li, H. Shi, Z. Wu, H. Huang, Z. Kang, Layered double hydroxide nanosheets activate CsPbBr3 nanocrystals for enhanced photocatalytic CO2 reduction, Nano Res. 15 (2022) 5953–5961.

[32] M. Humayun, C. Wang, W. Luo, Recent progress in the synthesis and applications of composite photocatalysts: a critical review, Small Methods 6 (2022), 2101395.

[33] S. Yang, X. Deng, P. Chen, G. Li, Q. Wang, Q. Wang, S.-F. Yin, Bridges engineering manipulated exciton dissociation and charge separation in small acceptors of PDI supramolecular for boosting photocatalytic nitrogen fixation, Chem. Eng. J. 441 (2022), 136084.

[34] R. Chandiramouli, A. Srivastava, V. Nagarajan, NO adsorption studies on silicene nanosheet: DFT investigation, Appl. Surf. Sci. 351 (2015) 662–672.

[35] W. Wei, S. Ouyang, T. Zhang, Perylene diimide self-assembly: from electronic structural modulation to photocatalytic applications, J. Semiconduct. 41 (2020), 091708.

[36] X. Xiong, C. Mao, Z. Yang, Q. Zhang, G.I.N. Waterhouse, L. Gu, T. Zhang, Photocatalytic CO2 reduction to CO over Ni single atoms supported on defect-rich zirconia, Adv. Energy Mater. 10 (2020) 2002928.

[37] H. Dong, L. Zhao, Y. Chen, M. Li, W. Chen, Y. Wang, X. Wei, Y. Zhang, Y. Zhou, M. Xu, Dual-ligand near-infrared luminescent lanthanide-based metal–organic framework coupled with in vivo microdialysis for highly sensitive ratiometric detection of Zn2+ in a mouse model of Alzheimer's disease, Anal. Chem. 94 (2022) 11940–11948.

[38] B.N. Ghosh, F. Topić, P.K. Sahoo, P. Mal, J. Linnera, E. Kalenius, H.M. Tuononen, K. Rissanen, Synthesis, structure and photophysical properties of a highly luminescent terpyridine-diphenylacetylene hybrid fluorophore and its metal complexes, Dalton Trans. 44 (2015) 254–267.

[39] P. Zhu, X. Yin, X. Gao, G. Dong, J. Xu, C. Wang, Enhanced photocatalytic NO removal and toxic NO2 production inhibition over ZIF-8-derived ZnO nanoparticles with controllable amount of oxygen vacancies, Chin. J. Catal. 42 (2021) 175–183.

[40] N. Zheng, X. He, W. Guo, Z. Hu, Enhancement of mass transfer efficiency and photoelectrochemical activity for TiO2 nanorod arrays by decorating Ni3+-states functional NiO water oxidation cocatalyst, Chin. Chem. Lett. 32 (2021) 1993–1997.

[41] Q. Zhang, S. Gao, Y. Guo, H. Wang, J. Wei, X. Su, H. Zhang, Z. Liu, J. Wang, Designing covalent organic frameworks with Co-O4 atomic sites for efficient CO2 photoreduction, Nature, Communications 14 (2023) 1147.

[42] S. Gao, Q. Zhang, X. Su, X. Wu, X.-G. Zhang, Y. Guo, Z. Li, J. Wei, H. Wang, S. Zhang, Ingenious artificial leaf based on covalent organic framework membranes for boosting CO2 photoreduction, J. Am. Chem. Soc. 145 (2023) 9520–9529.

[43] J. Ji, R. Li, H. Zhang, Y. Duan, Q. Liu, H. Wang, Z. Shen, Highly selective photocatalytic reduction of CO2 to ethane over Au-O-Ce sites at micro-interface, Appl. Catal. B Environ. 321 (2023), 122020.

[44] H. Zhang, Y. Li, J. Wang, N. Wu, H. Sheng, C. Chen, J. Zhao, An unprecedent hydride transfer pathway for selective photocatalytic reduction of CO2 to formic acid on TiO2, Appl. Catal. B Environ. 284 (2021), 119692.